Folding Panels of Uniform Thickness into Customised Shapes

Magnus Cheung

This report summarises the result of the author's Engineering Sciences final year project at Oxford University in 2024. The work would not have been possible without the excellent support of the supervisors, Dr. Jingyi Yang and Prof. Zhong You, who both provided inspiration and guidance throughout the year.

Abstract

Thick-panel spatial linkages have emerged as an alternative class of origami mechanisms for thick materials that aim to provide the same compact folding qualities as origami of zero-thickness sheets, but with improved engineering properties and consideration of material thickness.

Two new, distinct thick-panel mechanisms are presented in this report, both of which contain a degree of design flexibility that allows their folding form to be customised. The two mechanisms both maintain a uniform panel thickness and deploy with a single degree of freedom. Individually, both mechanisms generate new deployable structures with potential industrial applications. However, when combined, a more generalisable design scheme is found for customising the folded design of a flat-folding thick-panel array. This work brings the scope of thick-panel engineering design closer to the level of the well-established generalised zero-thickness origami design and is shown to be kinematically analogous to known origami mechanisms. Finally, the Appendix introduces a thick-panel, plane tiling, monohedral linkage that folds from a uniform-thickness sheet into a compact and regular folded state, with a single degree of freedom.

Contents

1. Introduction

1.1. Background

Origami has been a part of Japanese and Chinese cultures for many centuries, but recently the engineering applications of origami design have been sought out, particularly the controllability of single degree of freedom (DOF) deployment inherent to origami. Furthermore, origami-inspired designs excel in applications in which structures are deployed to a large size relative to their compact size during storage, i.e. a large packing ratio. This is exhibited in origami-inspired satellite arrays of antennae and solar panels [1] and remotely deployable miniature robots for biosensing and drug delivery [2].

At macro scales and under gravity, the thickness of origami materials must be great enough to support self-weight and external loads without buckling, however this limits the use of traditional creasing as they can no longer be considered simple revolute joints. To tackle this issue, a new field has emerged, dubbed 'Thick-panel origami', which aims to achieve a similar performance in packing ratio and controllability but with far greater structural integrity. Thickness is added to the faces of the origami mechanisms, which will henceforth be referred to as panels, and are connected to each other by joints rather than creases. These joints have improved fatigue resistance as the folds are enacted through hinges rather than bending membranes, however the design and positioning of these joints is not trivial and many solutions exist in the literature [3] [4] [5]. The kinematics of these joints and thick panels is, in most cases, different from the zero-thickness case, as the axes of revolute joints at a vertex longer necessarily meet at a single point, demonstrated in Figure 1a.

Of the several methods in the literature that tackle this issue, Offset Hinge [6], [7] is the technique used in this work, where a revolute joint is placed at top or bottom edges of the panels at each crease, so as to avoid panel collision when folding. Offset Hinge ensures the deployed state is guaranteed to be flat and the panels are all of uniform thickness. However, it is difficult to ensure the compact state is free of voids and collisions as the kinematics are not necessarily analogous to the underlying zero-thickness origami mechanism

The Offset Hinge technique, when applied to an origami crease pattern, can lead to overconstrained mechanisms. One approach to avoid this, developed by Wang et al 2018 [7], involves making cuts along edges or faces of panels to free some degrees of freedom and make the mechanism mobile, demonstrated in Figure 1b. This technique is more akin to the art of *kirigami*, and was dubbed 'Thick-Panel Kirigami' by Yang [8]. The mechanisms in this work fall under this technique.

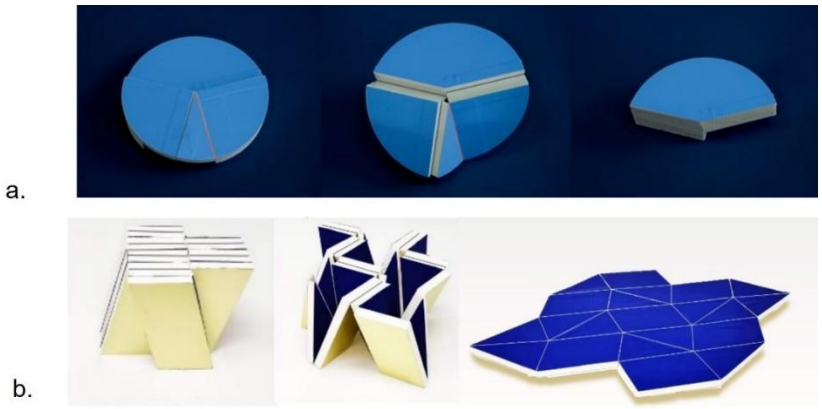

Figure 1 a. Folding of a thick-panel four-crease vertex from Chen et al 2015 [6]. b. A Thick-Panel Kirigami version of Miura-Ori from Yang 2022 [8]

1.2. Kinematic Analysis

The mechanisms analysed in this work are classed as rigid-body closed loop spatial linkages, for which it is typical to employ the Denavit-Hartenberg (D-H) Matrix method [9]. This method fully describes the motion of rigid-body mechanisms with a straightforward framework that can be applied to all spatial linkages composed of lower-pairs, such as revolute joints.

For each rigid body $\boldsymbol{P_i}$ in the spatial linkage comprising *n* rigid bodies, a coordinate system can be defined as follows: Z_i axes are placed along the axis of each revolute joint connecting bodies $\boldsymbol{P_{i-1}}$ and $\boldsymbol{P_i}$. X_i axes are placed along the perpendicular path between Z_{i-1} and Z_i. Since all linkages in this work are closed loop, with bodies numbered [1, 2...*n*], all instances of *i* - 1 and *i* + 1 outside this range can be taken modulo *n*. The D-H method uses the right-hand rule for all coordinate systems and no reflections are used here, so Y_i axes can be inferred from X_i and Z_i, however they are not used to any great extent in this work and are included for illustrative purposes only in all further analysis. When applying the D-H matrix method to Thick-Panel Kirigami, the Z_i axes are aligned with the joints between panels and the X_i axes are often aligned along the out of plane edges of the panels, along the "depth" direction.

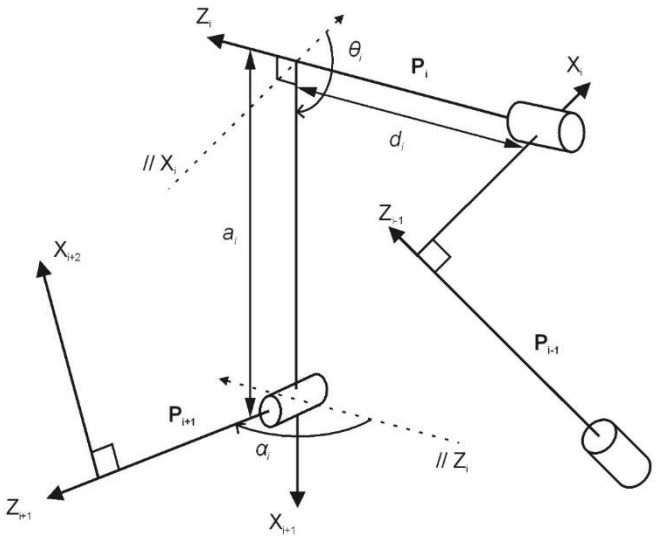

Figure 2 The kinematic variables for the i[th] rigid body in some spatial mechanism.

It can be shown that there are 4 independent parameters [d_i, θ_i, a_i, α_i] required to transform between any two 3D coordinate systems $X_iY_iZ_i \rightarrow X_{i+1}Y_{i+1}Z_{i+1}$. d_i, a_i and α_i are all constants and are defined by the panel geometry. θ_i is of most interest, as it captures the folding angles between panels and is the only variable that changes through the linkage motion. The 4x4 matrix $\boldsymbol{T}_{(i+1)i}$ is the combination of the 4 individual transformation associated with d_i, θ_i, a_i, α_i and transforms from a point in coordinate system *i* + 1 to system *i*.

$$\boldsymbol{T}_{(i+1)i} = \begin{bmatrix} \cos\theta_i & -\cos\alpha_i\sin\theta_i & \sin\alpha_i\sin\theta_i & a_i\cos\theta_i \\ \sin\theta_i & \cos\alpha_i\cos\theta_i & -\sin\alpha_i\cos\theta_i & a_i sin\theta_i \\ 0 & \sin\alpha_i & \cos\alpha_i & d_i \\ 0 & 0 & 0 & 1 \end{bmatrix}$$

For a closed-loop mechanism of *n* bodies, a point transformed through all *n* transforms $\boldsymbol{T}_{(i+1)i}$ must remain unchanged, hence the product of these transforms must be identity:

$$\prod_{i=1}^{n} \boldsymbol{T}_{(i+1)i} = \boldsymbol{I}$$

Satisfying this condition yields a set of 16 simultaneous equations in d_i, θ_i, a_i, and α_i , 12 of which are non-trivial and are known as the loop closure equations. The relations between angles θ_i that satisfy loop closure are called the kinematic or angle relations. For conceptual convenience, the angles θ are replaced with the dihedral angles φ between panels, which vary between $0 \leq \varphi \leq \pi$, unless otherwise stated.

2. Existing Mechanisms

This work builds on two known mechanisms in the field, the 6R and 8R linkages, which will be briefly presented here for clarity in later sections.

2.1. 6R Linkage

The 6R linkage can be derived from the common Chicken-wire origami crease pattern shown in Figure 3a. in which blue dashed lines represent valley folds, red dot dashed lines represent mountain folds and curved black lines represent a cut. By isolating a subsection of the crease pattern and introducing a slit in the centre, a 6-panel linkage is formed, highlighted in green and shown folding in 3D in Figure 3b. The geometry of the 6R linkages in this work, unless otherwise stated, will follow these conditions: The triangular panels are isosceles, with a common angle α^{6R} and a height w perpendicular to the sides of common length; the trapezoidal panels have a height w, a base twice the length of the triangular panels' common length and an acute angle of α^{6R}; all panels have a uniform thickness a. This geometry is captured in the D-H parameters below. It is worth noting that with these geometric constraints, small values of α^{6R} lead to the parallel sides of the trapezoidal panels becoming very long.

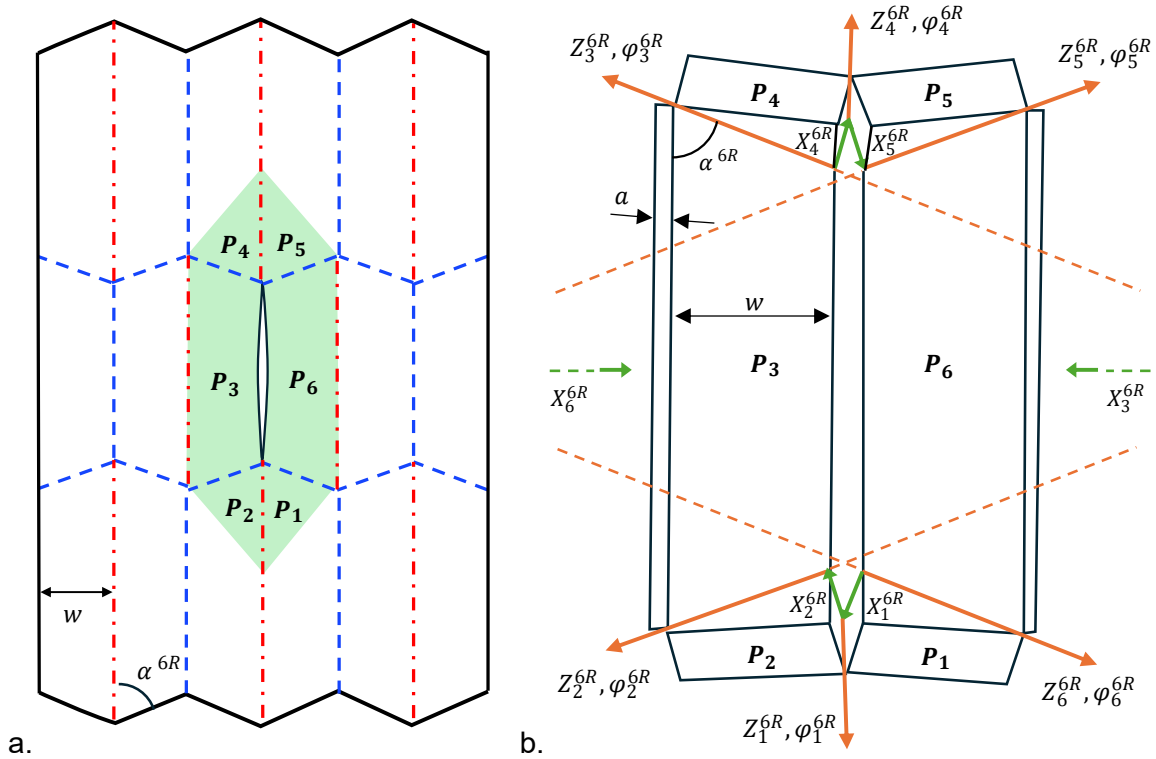

Figure 3 a. The 6R element and its topological diagram overlaid onto its parent crease pattern. b. The 6R element with its D-H axes.

The kinematic variables for this linkage are as follows:

$$d_1 = d_4 = 0 \qquad -d_2 = d_3 = -d_5 = d_6 = -\frac{w}{\tan 2\alpha_{6R} \cos \alpha^{6R}}$$

$$\theta_1 = -\varphi_1^{6R}, \quad \theta_2 = \varphi_2^{6R} - \pi, \quad \theta_3 = \varphi_3^{6R}, \quad \theta_4 = -\varphi_4^{6R}, \quad \theta_5 = \varphi_5^{6R} - \pi, \quad \theta_6 = \varphi_6^{6R}$$

$$a_1 = a_3 = a_4 = a_6 = a \qquad a_2 = a_5 = 0$$

$$-\alpha_1 = \alpha_3 = -\alpha_4 = \alpha_6 = \alpha^{6R} \qquad \alpha_2 = \alpha_4 = -\pi + 2\alpha^{6R}$$

The kinematics of the 6R linkage are well studied [10]; there exist three single DOF mobility paths (see Figure 4) for all the 6R mechanism described above, with a fourth path exhibited by a certain geometry discussed later. Path 1 is considered primary in this work, with Paths 2 and 3 as undesirable bifurcations.

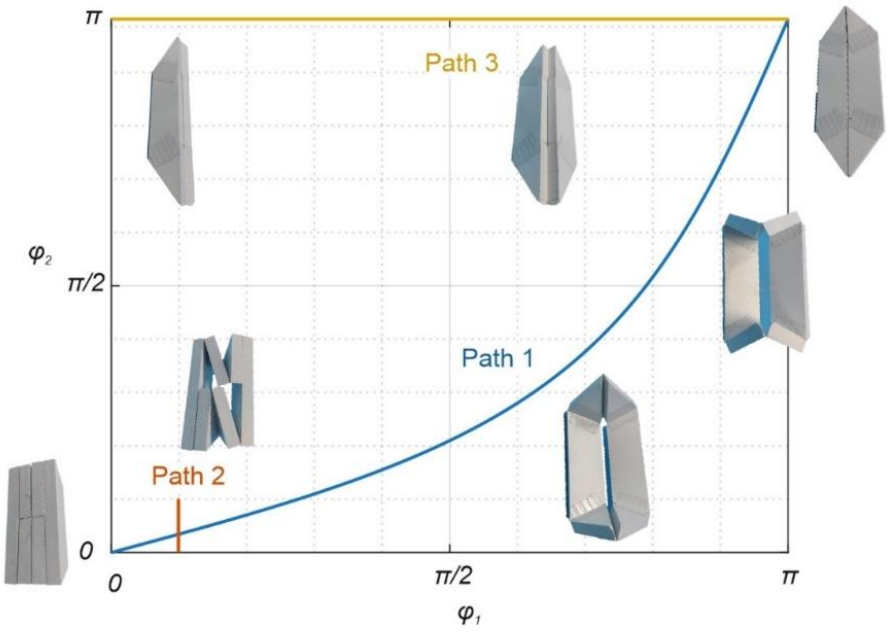

Figure 4. Three mobile Paths permissible by the 6R linkages in this work.

Path 1:

$$\varphi_1^{6R} = \varphi_4^{6R} = \varphi_2^{8R} = \varphi_4^{8R} = \varphi_6^{8R} = \varphi_8^{8R} \; ; \; \varphi_2^{6R} = \varphi_3^{6R} = \varphi_5^{6R} = \varphi_6^{6R} = \varphi_1^{8R} = \varphi_3^{8R} = \varphi_5^{8R} = \varphi_7^{8R}$$

$$\tan\frac{\varphi_1^{6R}}{2} = \cos\alpha^{6R} \tan\frac{\varphi_2^{6R}}{2}$$

Path 2:

$$\varphi_1^{6R} = \varphi_4^{6R} \; ; \; \varphi_2^{6R} = \varphi_5^{6R} \; ; \; \varphi_3^{6R} = \varphi_6^{6R} \; ; \; \tan\varphi_1^{6R} = \frac{4\sqrt{3}k}{4 - 3k^2} \; ; \; \tan\frac{\varphi_3^{6R}}{2} = \frac{2}{\sqrt{3}k} - \tan\frac{\varphi_2^{6R}}{2}$$

$$0 \le \varphi_2^{6R}, \varphi_3^{6R} \le 2\tan^{-1}\left(\frac{2}{\sqrt{3}k}\right) \; ; \; k = \frac{-2w}{a\tan(2\alpha^{6R})}$$

Path 3:

$$\varphi_1^{6R} = \varphi_4^{6R}, \quad \varphi_2^{6R} = \varphi_3^{6R} = \varphi_5^{6R} = \varphi_6^{6R} = 0$$

2.2. 8R Linkage

The 8R linkage can be derived from the Miura-Ori crease pattern shown in Figure 5a. By isolating a subsection of the crease pattern and introducing a slit in the centre, an 8-panel linkage is formed, highlighted in purple. The geometry of the 8R linkages in this work, unless otherwise stated, will follow these conditions: The triangular panels are isosceles, with a common angle α^{8R} and a height w perpendicular to the sides of common length; the parallelogram panels are formed by merging two of triangular panels; all panels have a uniform thickness a. This geometry is captured in the D-H parameters below and the spatial linkage is shown in Figure 5b.

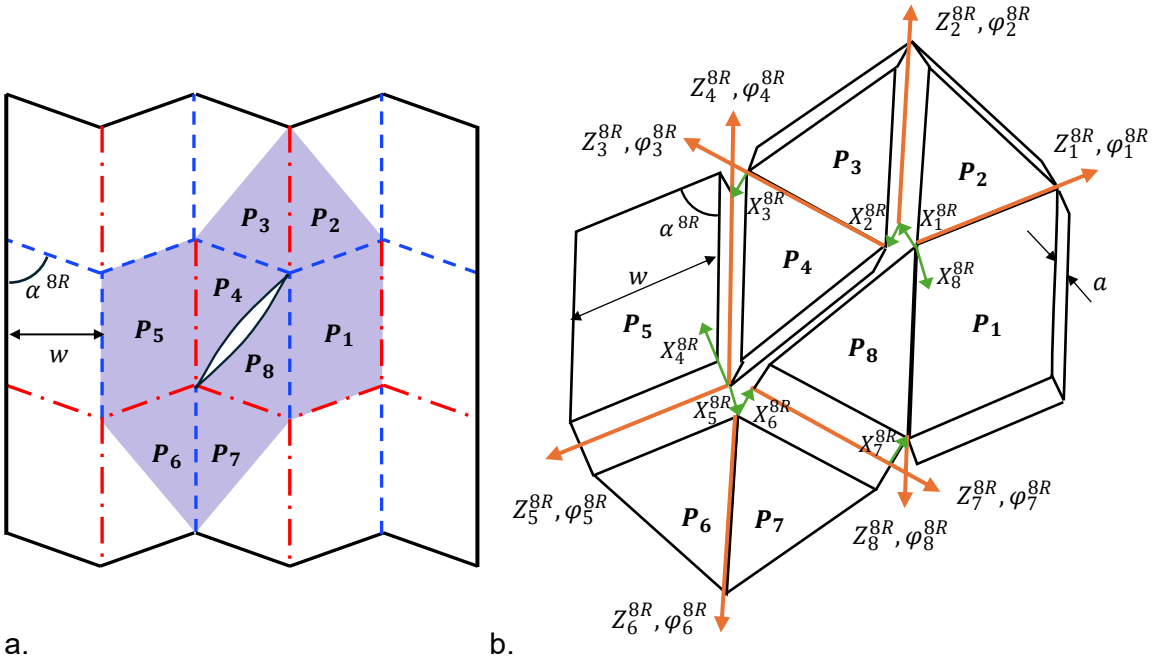

Figure 5a. The 8R element and its topological diagram overlaid onto its parent crease pattern. b. The 8R element with its D-H axes shown.

The kinematic variables for this linkage are as follows:

$$d_1 = d_2 = d_5 = d_6 = 0\ ;\ d_3 = d_7 = \frac{w}{\sin \alpha^{8R}}\ ;\ d_4 = d_8 = -\frac{w}{\sin(2\alpha^{8R})}$$

$$\theta_1 = \pi - \varphi_1^{8R}\ ;\ \theta_2 = \varphi_2^{8R}\ ;\ \theta_3 = -\varphi_3^{8R}\ ;\ \theta_4 = \varphi_4^{8R}\ ;\ \theta_5 = \varphi_5^{8R} - \pi\ ;\ \theta_6 = -\varphi_6^{8R}\ ;\ \theta_7 = \varphi_7^{8R}\ ;\ \theta_8 = -\varphi_8^{8R}$$

$$a_1 = a_2 = a_3 = a_5 = a_6 = a_7 = a\ ;\ a_4 = a_8 = 0$$

$$-\alpha_1 = \alpha_2 = \alpha_3 = \alpha_5 = -\alpha_6 = -\alpha_7 = \alpha^{8R}\ ;\ \alpha_4 = -\alpha_8 = \pi - \alpha^{8R}$$

The kinematics of the 8R linkage far less studied than the 6R; they have been numerically shown to have two DOFs, however the loop closure equations have not been solved analytically for a single 8R linkage. Some results have been found through the application of further constraints to the linkage, which will be discussed later.

3. Results

The novel developments of this work are outlined here and fall into three distinct subsections. The first two each cover a new thick-panel assembly, its geometry and kinematics, followed by a demonstration of its design capabilities. The last subsection then covers the result of combining the two assemblies, which successfully eliminates the individual short comings of each.

3.1. 6R8R Mechanism

The 6R8R assembly is formed by combining the two linkages described in Section 2. By merging overlapped panels of the corresponding 6R and 8R linkages, a combined mechanism is found.

3.1.1. Geometry and Kinematics

Given the geometric similarities between the Miura Ori and Chicken Wire crease patterns of identical w and α, it is simple to combine them, as shown in Figure 6a. Regarding the kinematics, the 8R linkage alone is not solved, however the introduction of the 6R linkage applies certain constraints on the motion. Firstly, the merging of the two linkages enforces the following angle relationships:

$$\varphi_3^{8R} = \varphi_3^{6R} \;\; ; \;\; \varphi_4^{8R} = \varphi_4^{6R}$$

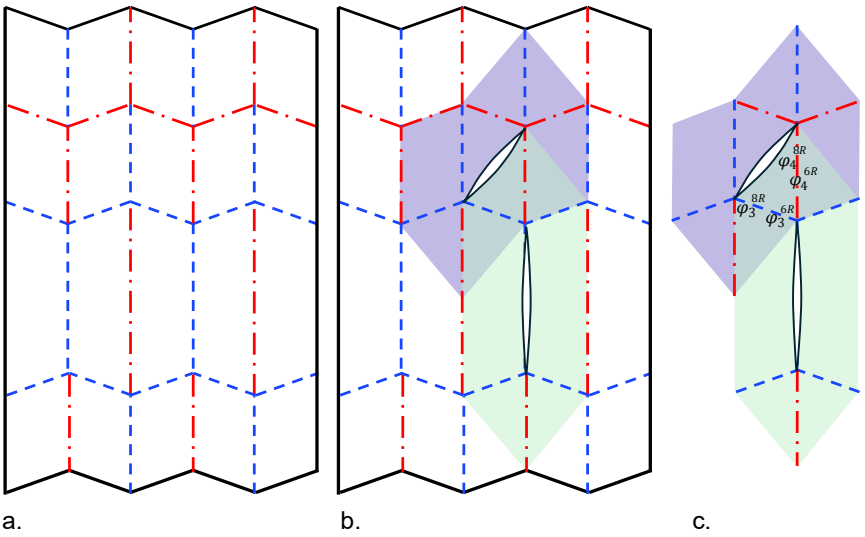

Figure 6a. The combined Miura Ori and Chicken Wire crease patterns. b. The corresponding 6R and 8R linkages superimposed on their crease patterns. c. The combined 6R8R mechanism.

It is apparent that the angles φ_3^{8R} and φ_4^{8R} are being driven by the single DOF 6R linkage. By considering the Path 1 motion of the 6R linkage the following relation must hold for the 8R linkage:

$$\tan\frac{\varphi_4^{8R}}{2} = \cos\alpha \tan\frac{\varphi_3^{8R}}{2}$$

This path is shown to be permissible by Yang 2022 [8]. The result found by Yang leads to a set of angle relations for the combined mechanism moving through Path 1 motion, which is shown in Figure 7 :

$$\varphi_1^{6R} = \varphi_4^{6R} = \varphi_2^{8R} = \varphi_4^{8R} = \varphi_6^{8R} = \varphi_8^{8R}$$

$$\varphi_2^{6R} = \varphi_3^{6R} = \varphi_5^{6R} = \varphi_6^{6R} = \varphi_1^{8R} = \varphi_3^{8R} = \varphi_5^{8R} = \varphi_7^{8R}$$

$$\tan\frac{\varphi_1^{6R}}{2} = \cos\alpha \tan\frac{\varphi_2^{6R}}{2}$$

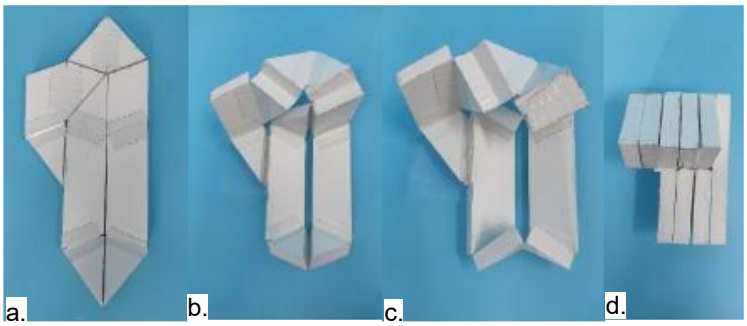

Figure 7a-d, 6R8R mechanism moving through Path 1, from $\varphi_1^{6R} = \pi \rightarrow 0$

Given how little is known about the kinematics of a single 8R linkage, it is difficult to demonstrate whether Paths 2 and 3 are permissible for the 8R6R linkage. Path 2 can, however, be eliminated by the addition of another 8R linkage on the other end of the 6R linkage, as shown in Figure 8. The top and bottom 8R linkages are referred to in superscripts as 8Ra and 8Rb respectively.

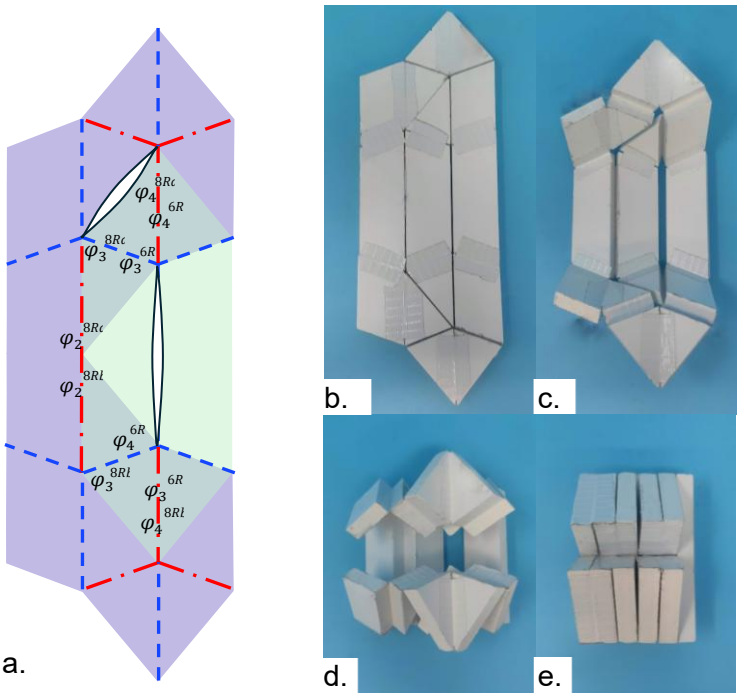

Figure 8a. 8R6R8R mechanism, with shared dihedral angles shown. b. The compact topological diagram of the mechanism. c-f. The 8R6R8R mechanism moving through Path 1 motion.

When moving through Path 2, the two DOFs of the 8R linkages will be fully defined by the 6R linkage as follows:

$$\tan\varphi_4^{8\mathrm{Ra}} = \tan\varphi_4^{8\mathrm{Rb}} = \frac{4\sqrt{3}k}{4-3k^2} \;\; ; \;\; \tan\frac{\varphi_3^{8\mathrm{Ra}}}{2} = \frac{2}{\sqrt{3}k} - \tan\frac{\varphi_3^{8\mathrm{Rb}}}{2} \; ; \; k = \frac{-2w}{a\tan(2\alpha)}$$

Since the 8R linkages have two DOFs and with both $\varphi_4^{8\mathrm{Ra}}$ and $\varphi_4^{8\mathrm{Rb}}$ fixed, there exists some function h for which $\varphi_2^{8\mathrm{R}} = h(\varphi_3^{8\mathrm{R}})$, that applies to both 8R linkages since they are reflections of one another. It is assumed that $h(\varphi_3^{8\mathrm{R}})$ is monotonic in the range $0 \leq \varphi_3^{8R} \leq 2\tan^{-1}\left(\frac{2}{\sqrt{3}k}\right)$, which can be confirmed by

experiment. Therefore, $h(\varphi_3^{8\mathrm{Ra}}) \neq h\left(2tan^{-1}\left(\frac{2}{\sqrt{3}k} - \tan\frac{\varphi_3^{8\mathrm{Rb}}}{2}\right)\right)$ with the exception of $\varphi_3^{8\mathrm{Ra}} = \varphi_3^{8\mathrm{Rb}} = 2\tan^{-1}\left(\frac{1}{\sqrt{3}k}\right)$, hence $\varphi_2^{8\mathrm{Ra}} \neq \varphi_2^{8\mathrm{Rb}}$ in general, outside of that one value for $\varphi_3^{8\mathrm{Ra}}$ and $\varphi_3^{8\mathrm{Rb}}$. From Figure 8a it is clear that $\varphi_2^{8\mathrm{Ra}} = \varphi_2^{8\mathrm{Rb}}$, so Path 2 motion cannot be permitted.

Path 3 motion is less clear; experimentally it is not permissible for 6R8R, but for analytical confirmation it would require the loop closure equations for the 8R linkage to be solved with $\varphi_3^{8\mathrm{R}} = 0$, effectively creating a 7R linkage with the same geometry.

3.1.2. Resulting 6R8R Assemblies

By considering a 6R linkage as a single DOF "driver" linkage and appending 8R linkages, as in Figure 9, the 8R linkages directly adjacent to the 6R linkage are driven through Path 1 motion with a single DOF, as discussed above. Further 8R linkages added to either end of the 8R6R8R linkage follow the same motion, being driven by the inner 8R linkages, following the same logic as above. In the folded state, the arrays of 8R linkages will be rotated by angle $\delta = 2\alpha$ relative to one another, as shown in Figure 9. This concept is explored in the two example assemblies below.

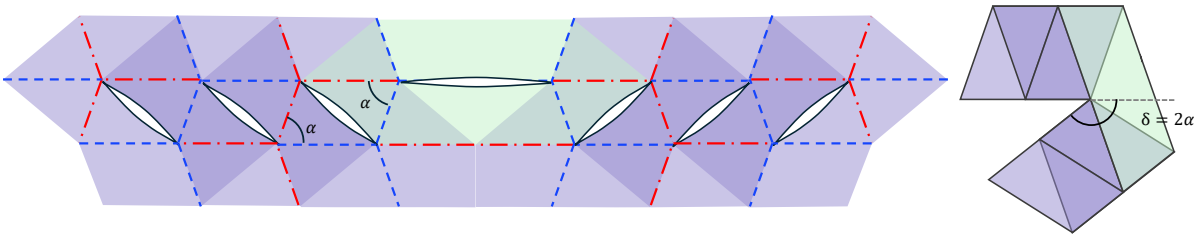

Figure 9. Unfolded and folded states of the combined array.

Both the 6R8R assemblies are single degree of freedom assemblies, with uniform, voidless unfolded forms. They have fairly regular unfolded and folded forms, the dimensions of which can be adjusted in both width and length with the simple addition of rows or linkages, respectively.

3.1.2.1. 6R8R Square

Let the sector angle $\alpha = \frac{\pi}{4}$, so the turning angle, δ, induced by the 6R linkages will be $\frac{\pi}{2}$. The corresponding 8R and 6R linkages are shown in Figure 10a. and b. Note that the 6R linkage here has zero slit length, this results in a fully compact folded state and two additional motion paths. The alignment of the Z_2^{6R} and Z_5^{6R} axes and Z_3^{6R} and Z_6^{6R} axes allows the linkage to fold along both combined axes. This motion is classed as a fourth motion path and can introduce another bifurcation to assemblies, however it can be eliminated if the combined axis is interrupted.

Path 4a.

$$\varphi_2^{6\mathrm{R}} = \varphi_5^{6\mathrm{R}}, \quad \varphi_1^{6\mathrm{R}} = \varphi_3^{6\mathrm{R}} = \varphi_4^{6\mathrm{R}} = \varphi_6^{6\mathrm{R}} = 0$$

Path 4b.

$$\varphi_3^{6\mathrm{R}} = \varphi_6^{6\mathrm{R}}, \quad \varphi_1^{6\mathrm{R}} = \varphi_2^{6\mathrm{R}} = \varphi_5^{6\mathrm{R}} = \varphi_6^{6\mathrm{R}} = 0$$

Eight of these 8R linkages and three 6R linkages can be combined into the arrangement shown in Figure 10c. Note that the combined Z_3^{6R} and Z_6^{6R} axes of each 6R linkage are interrupted by panels from the 8R linkages and as such cannot exhibit Path 4 motion.

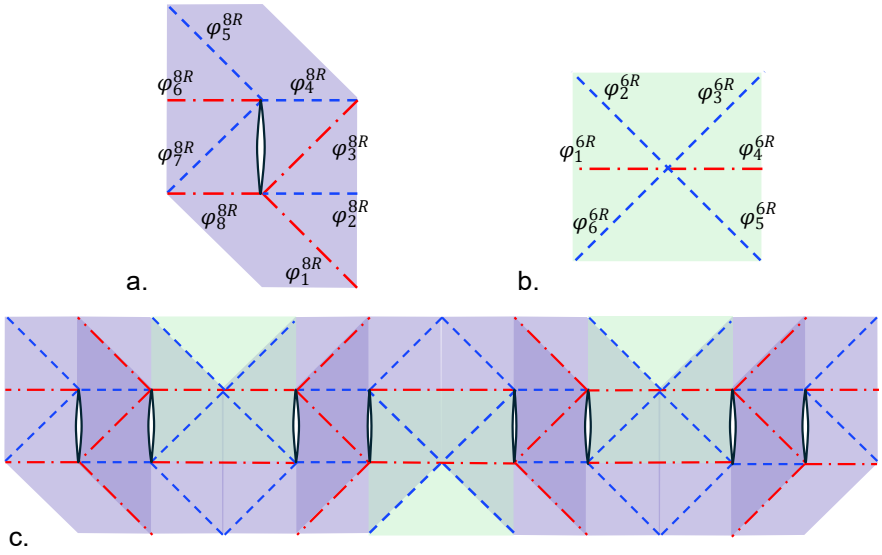

Figure 10a. 8R linkage with $\alpha = 45°$ b. 6R linkage with $\alpha = 45°$ c. Combined array of 8R and 6R linkages. d. Concise topological diagram of the assembly.

The motion of this assembly can be found by treating the central 6R linkage as the single DOF input to the assembly. It is apparent that the two DOFs of each adjacent 8R linkage are fully defined, as previously shown, and the motion of all the linkages can be found in a similar manner, since all adjacent linkages are driven according to the same argument, resulting in a single DOF deployment as shown in Figure 11. Due to its construction from purely 8R and 6R linkages, the unfolded state of this assembly is uniform thickness and without holes. The folded state of this assembly has a square footprint, so many copies could pack a plane, albeit with regular square holes included. At each 8R pair in Figure 10c, a further even number of 8R linkages can be introduced, following the existing overlapping pattern. The mobility of these new linkages will also follow Path 1 motion, as they share three joints with their neighbours, fully constraining them to this Path. The resultant assembly will have increased unfolded length and will fold into a square of greater side length. Furthermore, by observing the repetition of the top and bottom rows in Figure 10c, it can be seen that the width can be increased with the addition of further rows in increments of two. By noting the similarities between the top and bottom rows of the crease pattern in Figure 10c, the pattern can be duplicated in this direction and would lead to an increase height along the axis of the hole in the folded state. This relationship also allows copies of the assembly to be stacked in their folded form.

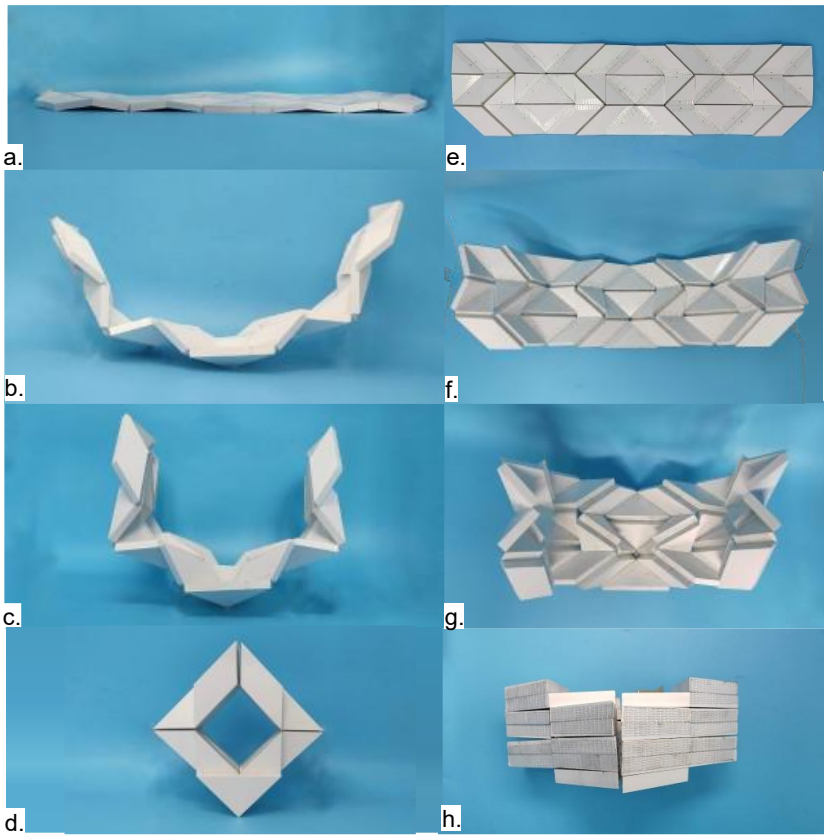

Figure 11. The 6R8R assembly moving from flat to folded state. a-d Profile view. e-h Plan view.

3.1.2.2. 6R8R Snake Assembly

Using the same linkage geometry as shown in Figure 10a, a different arrangement of three 8R and four 6R linkages shown in Figure 12. Each pair of 6R linkages introduces a , $\delta = \pi$ turning angle, allowing the folded form to fold back on itself, hence the "Snake" Assembly. The folded form of this assembly is regular in shape and has no voids, making it particularly useful for compact storage. Further pairs of 8R elements can be added between each 6R pair in a manner similar to the Square Assembly. The resultant assembly would have increase length in both the folded and unfolded state. Note that each pair of overlapped 6R linkages now share a common crease, thereby permitting Path 4 motion, as shown in Figure 12. While bifurcations are typically unwanted in controllable mechanisms, Path 4 does present an alternative folded form shape, which could be of interest. As with the Square assembly, pairs of rows can be added to the pattern shown in Figure 12, having the effect of increasing the width of both the folded and folded forms.

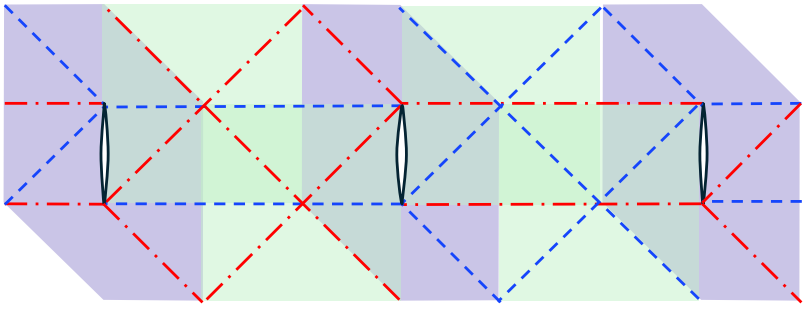

Figure 12. Combined array of 8R and 6R linkages.

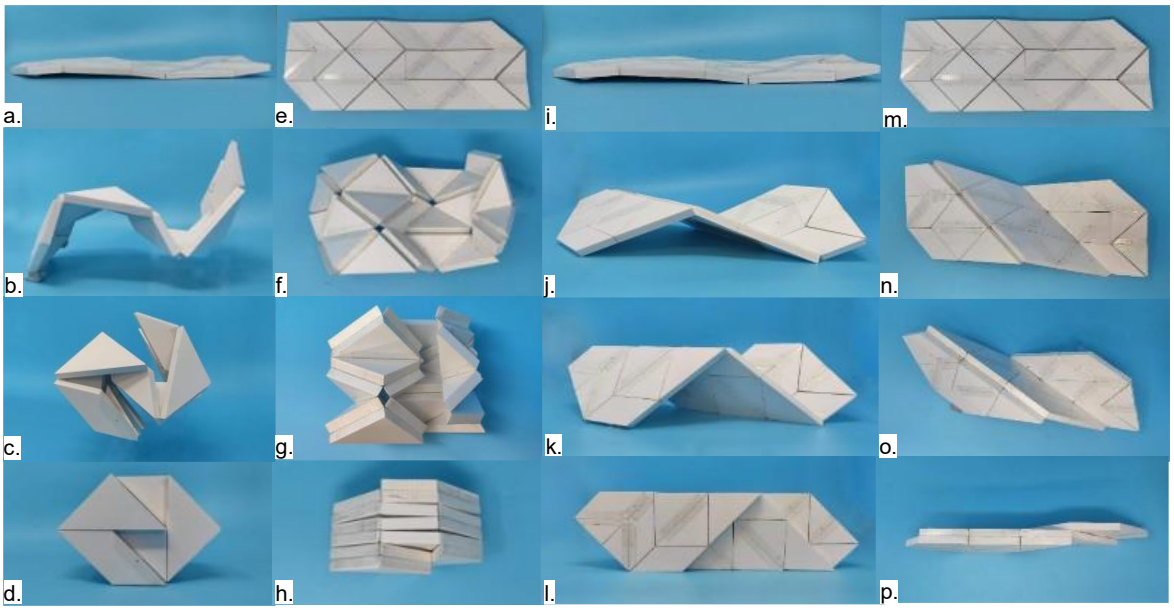

Figure 13. Snake Assembly folding up via Path 1 motion. a-d, side view. e-h. plan view. Snake Assembly displaying Path 4 motion, i-l. side view, m-p. plan view.

3.2. Arc Miura

3.2.1. Geometry and Kinematics

The kinematics of zero thickness variants of the Miura Ori pattern have been well-explored. One variant, referred to here as "Arc Miura" is shown in Figure 14.

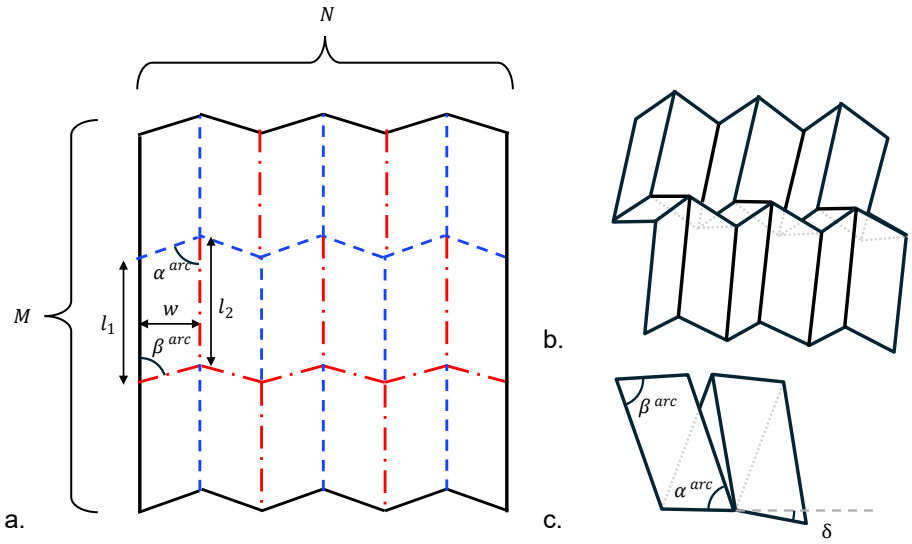

Figure 14. a. Arc Miura crease pattern, b. Arc Miura folding, c. The folded state of Arc Miura.

This more generalised version of Miura Ori leaves certain geometries undefined, so some constraints must be applied if a Thick-Panel Arc Miura is to be developed from this pattern.

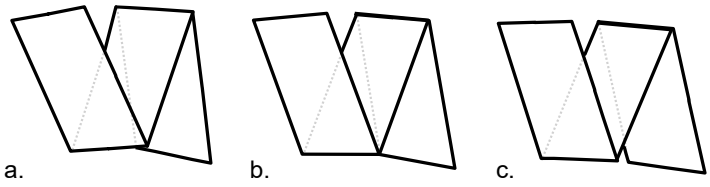

Figure 15. Three possible geometries of zero-thickness Arc Miura.

Firstly, by observing the lower edges in Figure 15, geometry *a* can be discounted as a collision of layers would occur here. Secondly, to minimise the void volume in the folded state, geometry *c* can be discounted. The exact meeting of panels at the turning point in geometry *b* is fully defined and the turning angle is given in Figure 16a.

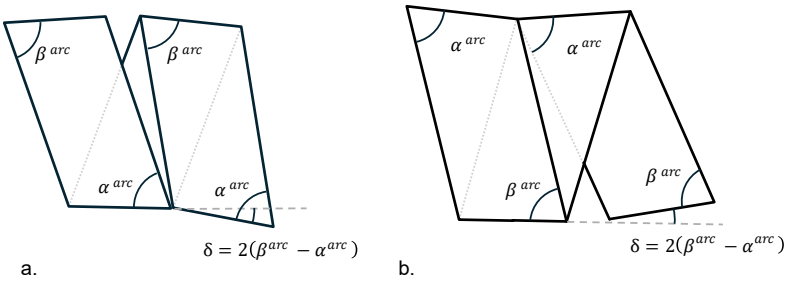

Figure 16a. The geometry of the Arc Miura folded state. b. The geometry of the same pattern, upside down.

Next, consider a single column of faces Figure 14a in their unfolded state as a straight strip of paper. Each crease in the pattern turns the strip up by β^{arc} or down by α^{arc} in the folded state. Since the angle between the two opposite, non-parallel edges in a single face are at an angle of $\beta^{arc} - \alpha^{arc}$, the angle developed by a fold upwards then downwards will be $\delta = 2(\beta^{arc} - \alpha^{arc})$.

Furthermore, considering the case for $\delta < 0$, the resultant geometry is equivalent to turning the model upside down, which gives the same result with $\delta > 0$ by switching α^{arc} and β^{arc}, as demonstrated in Figure 16b. Hence only $\delta \geq 0$ will be considered here.

Using this geometry, the kinematics of the zero thickness case can be derived using the well-known [11] result for the 4 crease vertex.

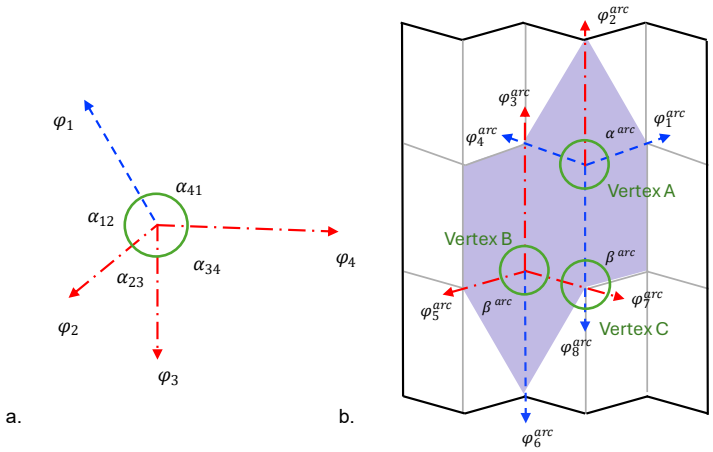

Figure 17a. The general 4 crease vertex, as denoted by Xing [11], b. The vertices of interest in the Arc Miura crease pattern.

$$\varphi_1 = \varphi_3, \qquad \varphi_2 = \varphi_4, \qquad \sin\frac{\alpha_{12} - \alpha_{23}}{2}\tan\frac{\varphi_1}{2} = \sin\frac{\alpha_{12} + \alpha_{23}}{2}\tan\frac{\varphi_2}{2}$$

By substituting values the relevant values of α^{arc} and β^{arc} into the system above, Vertex A is described with the following equations, relating $\varphi_1^{\text{arc}}, \varphi_2^{\text{arc}}, \varphi_3^{\text{arc}}$and φ_8^{arc} with each other.

$$\varphi_1^{\text{arc}} = \varphi_3^{\text{arc}}, \qquad \varphi_2^{\text{arc}} = \varphi_8^{\text{arc}}, \qquad \tan\frac{\varphi_1^{\text{arc}}}{2} = \cos\alpha^{arc}\tan\frac{\varphi_8^{\text{arc}}}{2}$$

Similarly, Vertex B is described with the following equations, relating $\varphi_4^{\text{arc}}, \varphi_5^{\text{arc}}, \varphi_6^{\text{arc}}$and φ_7^{arc} with each other.

$$\varphi_5^{\text{arc}} = \varphi_7^{\text{arc}}, \qquad \varphi_6^{\text{arc}} = \varphi_4^{\text{arc}}, \qquad \tan\frac{\varphi_5^{\text{arc}}}{2} = \cos\beta^{arc}\tan\frac{\varphi_7^{\text{arc}}}{2}$$

By observing Vertex C, a relation between φ_1^{arc} and φ_5^{arc} is found, unifying the loop closure equations for the 8R linkage.

$$\tan\frac{\varphi_7^{\text{arc}}}{2} = \cos\beta^{arc}\tan\frac{\varphi_8^{\text{arc}}}{2} = \frac{\cos\beta^{arc}}{\cos\alpha^{arc}}\tan\frac{\varphi_1^{\text{arc}}}{2} = \tan\frac{\varphi_5^{\text{arc}}}{2}$$

The Thick-Panel Kirigami Arc 8R linkage can be constructed in a similar manner to the 8R linkage discussed in Section 2.2, as shown in Figure 18, the D-H geometry of which is given below. Clearly the geometry collapses back to Yang's 8R linkage when $\alpha^{arc} = \beta^{arc}$ i.e. $\delta^{arc} = 0$. Note that, for large values of δ^{arc}, β^{arc} approaches $\frac{\pi}{2}$, leading to very elongated panels, so for large turning angles δ^{arc} the panel geometry becomes impractical for engineering design.

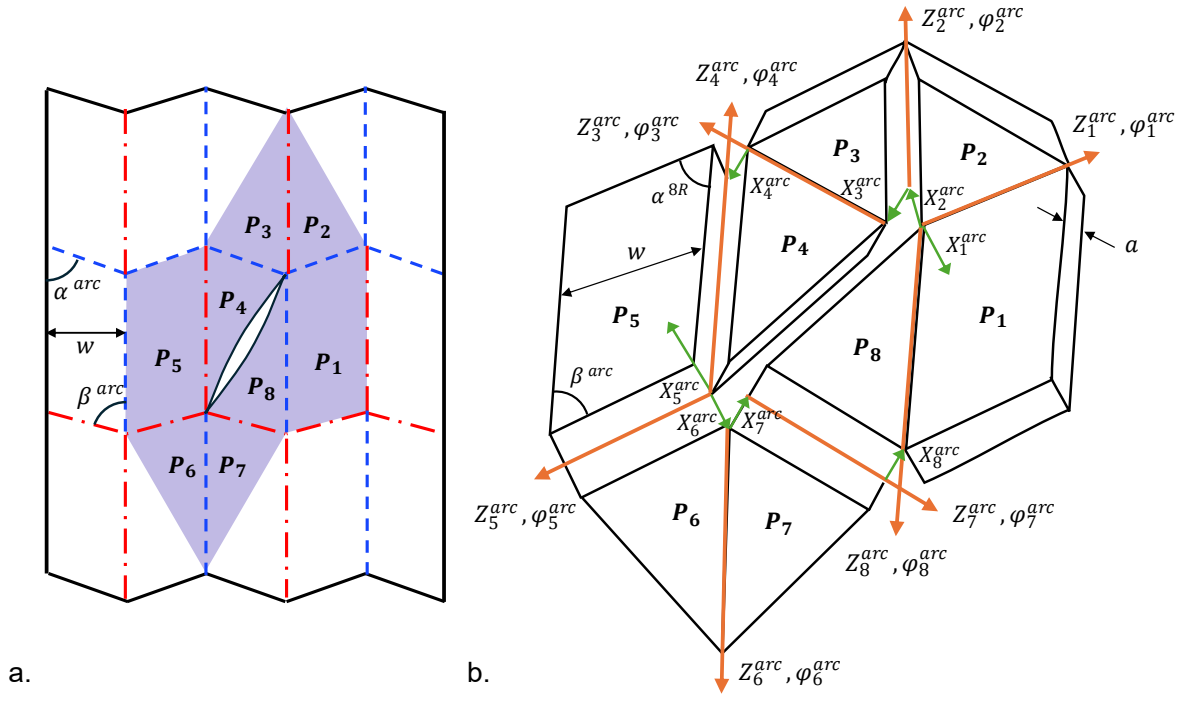

Figure 18. The Arc 8R element and its topological diagram overlaid onto its parent crease pattern. b. The Arc 8R element with its D-H axes

$$d_1 = d_2 = d_5 = d_6 = 0, \quad d_3 = \frac{w}{\sin \alpha^{arc}}, \quad d_4 = -w(\cot \alpha^{arc} - \cot 2\beta^{arc}),$$

$$d_7 = \frac{w}{\sin \beta^{arc}}, \quad d_8 = \frac{-w}{\sin(2\beta^{arc})}$$

$$\theta_1 = \pi - \varphi_1^{\text{arc}}, \quad \theta_2 = \varphi_2^{\text{arc}}, \quad \theta_3 = -\varphi_3^{\text{arc}}, \quad \theta_4 = \varphi_4^{\text{arc}}$$

$$\theta_5 = \varphi_5^{\text{arc}} - \pi, \quad \theta_6 = -\varphi_6^{\text{arc}}, \quad \theta_7 = \varphi_7^{\text{arc}}, \quad \theta_8 = -\varphi_8^{\text{arc}}$$

$$a_1 = a_2 = a_3 = a_5 = a_6 = a_7 = a, \quad a_4 = a_8 = 0$$

$$-\alpha_1 = \alpha_2 = \alpha_3 = \alpha^{arc}, \quad \alpha_4 = \pi - \beta^{arc}, \quad \alpha_5 = -\alpha_6 = -\alpha_7 = \beta^{arc}, \quad \alpha_8 = \alpha^{arc} - \pi$$

A key property of the Arc 8R linkage is its chirality; it is a distinct mechanism to its reflection and as such must be treated separately. The “standard” Arc 8R linkage will be coloured purple going forward. The reflected linkage is demarked with “primed” geometry and will be coloured blue, as shown in in Figure 19.

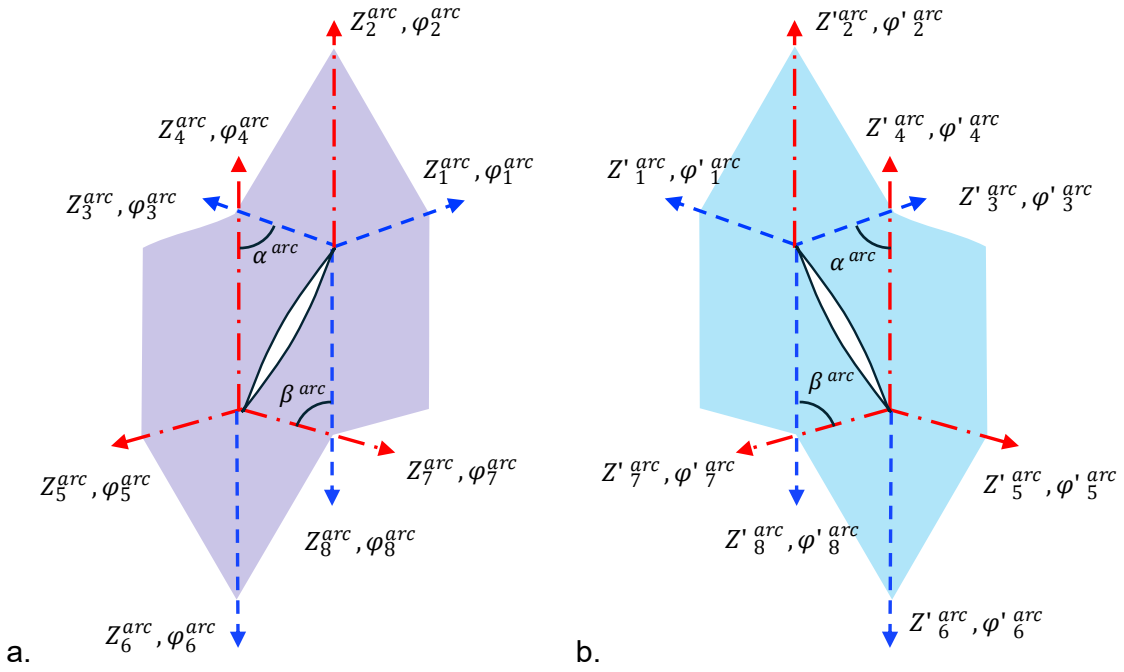

Figure 19a. An Arc 8R linkage. b. The reflected linkage, with "primed" geometry.

Using these Arc 8R linkages, an assembly can be formed following the same method as Yang 2022, as shown in Figure 20. Many of the assumptions they made during their analysis will be repeated here as the Arc 8R linkages behave in a similar manner to Yang 2022 [8].

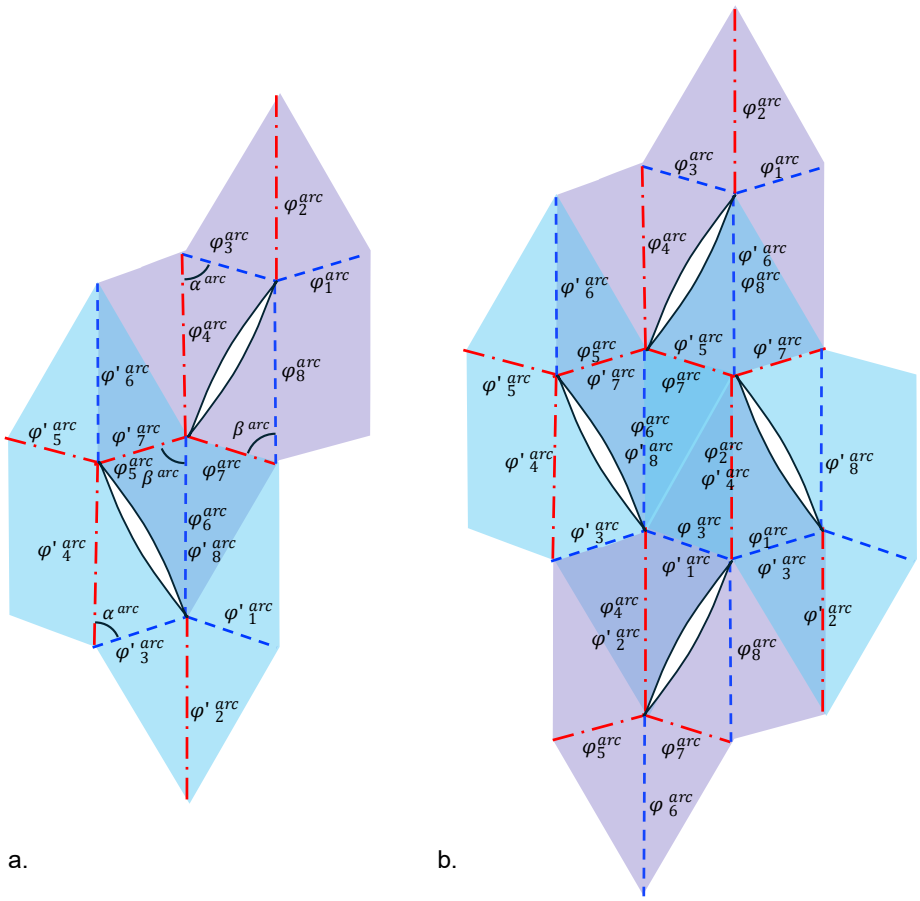

Figure 20a. Two Arc 8R linkages combined. b. Four Arc 8R linkages combined.

Firstly, it is assumed that all the Arc 8R linkages follow the same mobility path, albeit reflected for the "primed" linkages, hence $\varphi_i^{\text{arc}} = \varphi_i^{\text{arc}\prime}$. By observing the shared joints in the assembly, it is clear that the following relations hold:

$$\varphi_1^{\text{arc}} = \varphi_3^{\text{arc}}, \quad \varphi_2^{\text{arc}} = \varphi_4^{\text{arc}}, \quad \varphi_5^{\text{arc}} = \varphi_7^{\text{arc}}, \quad \varphi_6^{\text{arc}} = \varphi_8^{\text{arc}}$$

The second assumption is that each end of the Arc 8R linkages behaves like the regular 8R linkage of that end's geometry and follows Path 1 motion. This assumption is based on the behaviour of physical and simulated models of the assembly.

$$\tan\frac{\varphi_1^{\text{arc}}}{2} = \cos\alpha^{arc}\tan\frac{\varphi_2^{\text{arc}}}{2}, \quad \tan\frac{\varphi_5^{\text{arc}}}{2} = \cos\beta^{arc}\tan\frac{\varphi_6^{\text{arc}}}{2}$$

The final assumption is that the panels on either side of the slit in each Arc 8R linkage remain parallel to one another. This assumption is again based on the behaviour of physical and simulated models of the assembly. This would imply that the unit vectors parallel to ${X_4}^{arc}$ and ${X_8}^{arc}$ in Figure 18 would sum to the zero vector.

$$\hat{X}_4^{\ arc} + \hat{X}_8^{\ arc} = \mathbf{0}$$

These unit vectors can be constructed through repeated transformations of the global unit vector in the ${X_1}^{arc}$ direction.

$$(\boldsymbol{T_{21}} \cdot \boldsymbol{T_{32}} \cdot \boldsymbol{T_{43}} + \boldsymbol{T_{81}}) \cdot [1,0,0,0]^T = \mathbf{0}$$

Substituting the existing relations above into the expressions for the transformation matrices and inspecting the first element in the resultant vector gives the following:

$$\left(\tan\frac{\varphi_1^{\mathrm{arc}}}{2}\right)^2-\left(\tan\frac{\varphi_5^{\mathrm{arc}}}{2}\right)^2-\left(\tan\frac{\varphi_5^{\mathrm{arc}}}{2}\right)^2\cos(2\alpha^{arc})+\left(\tan\frac{\varphi_1^{\mathrm{arc}}}{2}\right)^2\cos(2\beta^{arc})=0$$

This can be simplified into a final angle relation between φ_1^{arc} and φ_5^{arc}, reducing the degrees of freedom of the system to one.

$$\tan\frac{\varphi_5^{\mathrm{arc}}}{2}=\sqrt{\frac{1+\cos(2\beta^{arc})}{1+\cos(2\alpha^{arc})}}\tan\frac{\varphi_1^{\mathrm{arc}}}{2}=\frac{\cos\beta^{arc}}{\cos\alpha^{arc}}\tan\frac{\varphi_1^{\mathrm{arc}}}{2}$$

Substituting all these relations into the loop closure equations does return unity and therefore represent a valid kinematic path for the Arc 8R assembly.

$$\varphi_1^{\mathrm{arc}}=\varphi_3^{\mathrm{arc}},\quad \varphi_2^{\mathrm{arc}}=\varphi_4^{\mathrm{arc}},\quad \varphi_5^{\mathrm{arc}}=\varphi_7^{\mathrm{arc}},\quad \varphi_6^{\mathrm{arc}}=\varphi_8^{\mathrm{arc}}$$

$$\tan\frac{\varphi_1^{\mathrm{arc}}}{2}=\cos\alpha^{arc}\tan\frac{\varphi_2^{\mathrm{arc}}}{2},\quad \tan\frac{\varphi_5^{\mathrm{arc}}}{2}=\cos\beta^{arc}\tan\frac{\varphi_6^{\mathrm{arc}}}{2}$$

$$\tan\frac{\varphi_5^{\mathrm{arc}}}{2}=\frac{\cos\beta^{arc}}{\cos\alpha^{arc}}\tan\frac{\varphi_1^{\mathrm{arc}}}{2}$$

This path is kinematically analogous to the zero-thickness case, and as such this assembly can be considered a thick panel version of the Arc Miura pattern. The assembly in Figure 21 has $\alpha^{arc}=\frac{7\pi}{18}, \delta^{arc}=\frac{\pi}{18}$.

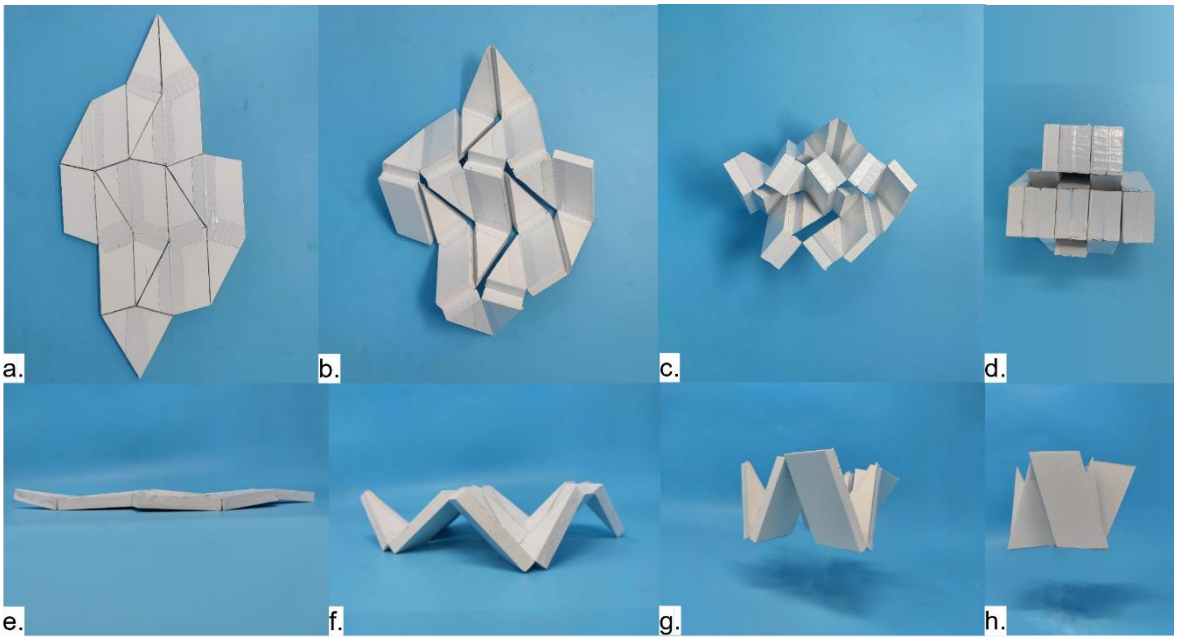

Figure 21 The Arc Miura assembly moving through Path 1 motion a-d. plan view, e-h. side view.

3.2.2. Design flexibility and limitations

A simple example of how this assembly is to repeat the pattern, leading to a constant turning angle, or curvature, in the folded state. Using $\alpha^{arc} = \frac{\pi}{4}$ and $\delta^{arc} = \frac{\pi}{18}$, each unit will turn $\frac{\pi}{18}$ so combining 36 units into one assembly, dubbed the "Circle Assembly" results in a full circular folded state, as shown in Figure 22.

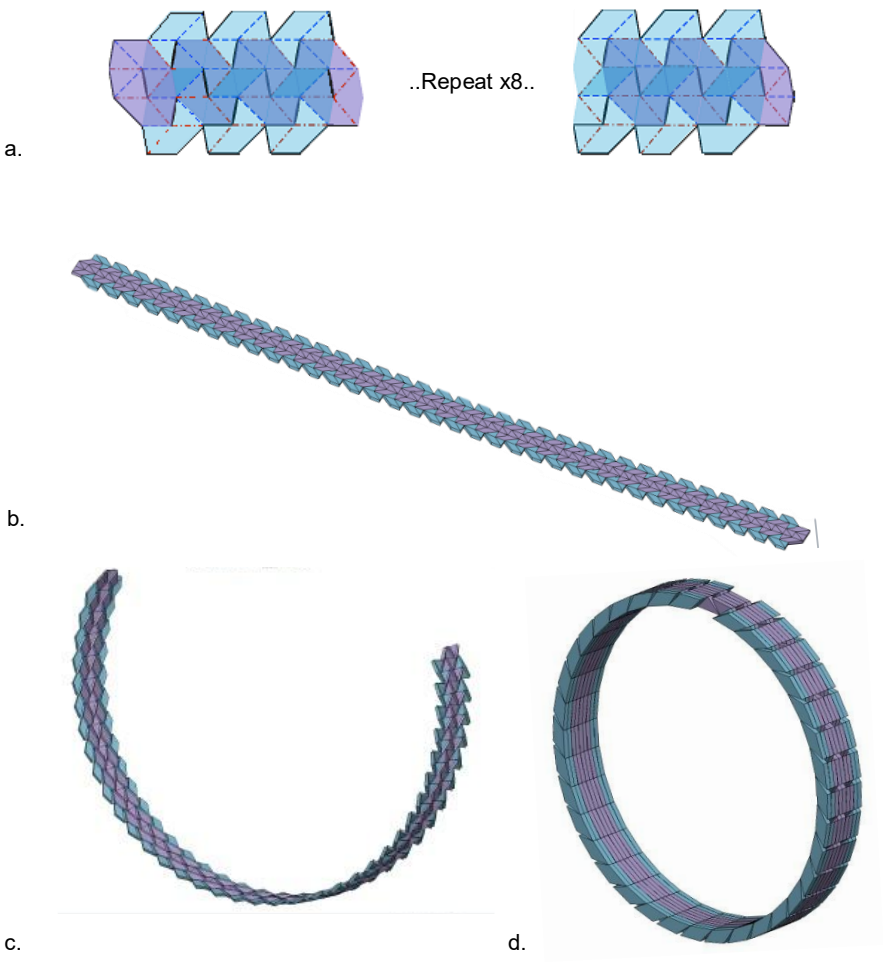

Figure 22a. An abridged crease pattern the Circle assembly is based on. b-d. The Circle assembly moving through Path 1 motion from unfolded to folded.

The values for α^{arc} and δ^{arc} determine the curve followed by the folded form and the kinematics do not disallow any values for either variable any more than the physical geometry ($\alpha^{arc} < \frac{\pi}{2}$ and $\beta^{arc} < \frac{\pi}{2}$) However, an additional constraint on the geometry can be found by investigating the surfaces at the slit. They are coplanar in the unfolded state, and separate through Path 1 motion, with the perpendicular distance given below as p.

$$p = -\frac{4\tan\left(\frac{\varphi_1^{\text{arc}}}{2}\right)\cos(\alpha^{arc})\cos(2\beta^{arc})}{1 + 2\tan^2\left(\frac{\varphi_1^{\text{arc}}}{2}\right) + \cos(2\alpha^{arc})}a \geq 0$$

Constraining p to remain positive through the range $0 < \varphi_1^{\text{arc}} < \pi$ ensures there will be no collisions between panels $\boldsymbol{P_4}$ and $\boldsymbol{P_8}$. Given $0 < \alpha^{arc} < \frac{\pi}{2}$, only the $\cos(2\beta^{arc})$ term can lead to $p < 0$, hence the condition:

$$\beta^{arc} \geq \frac{\pi}{4}$$

Leading to bounds on α^{arc} and β^{arc} :

$$0 < \alpha^{arc} < \frac{\pi}{2} \quad ; \quad \frac{\pi}{4} \leq \beta^{arc} < \frac{\pi}{2} \quad ; \quad 0 \leq \delta \leq \frac{\pi}{2}$$

Given the generalised nature of the geometry and kinematics, values for δ can be chosen freely between 0 and $\frac{\pi}{2}$. Furthermore, by following the method described in Section 3.2.1, the folded state can effectively be turned through negative values of δ, and as such can follow any continuous function in the 2D plane. This capability is trivial for the zero-thickness case but is now extended to Thick-Panel Kirigami. However, while these ranges for α^{arc} and β^{arc} describe what is physically possible, large values of β^{arc} lead to panel side lengths becoming unreasonably long, so designing assemblies with large values of δ become impractical. Limiting the short diagonal of the characteristic panel to $2w$, leads to an adjusted upper bound, $\beta^{arc} \leq \frac{5\pi}{12}$, then by the enforcing positive δ, then $\alpha^{arc} < \frac{5\pi}{12}$.

3.3. Combined Mechanisms

While both assemblies discussed above have a range of design freedom, they each have limitations on either ends of the turning angles they can achieve without significantly lengthening their geometry, as shown in Figure 23. However, since both assemblies are based on the similar geometries, they can be combined easily and avoid the other's limitations.

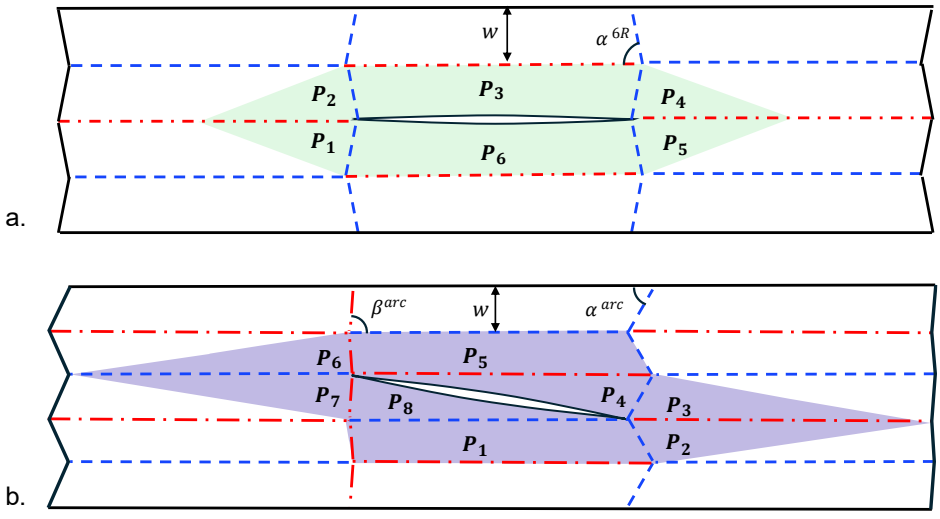

Figure 23a. 6R linkage for a small δ, b. Arc 8R linkage achieving a large δ.

An array of Yang's 8R linkages with identical values of α has a folded state that will follow a straight line, i.e. $\delta = 0$ everywhere. By introducing a row of Arc 8R linkages, the geometry changes across the central panels from α^{array} to β^{arc} for a single row, inducing a turning angle $\delta = 2(\beta^{arc} - \alpha^{array})$ in the folded state before it returns to a straight line. The framework of a turning angle per row of panels can also be applied to the 6R8R assembly, where $\delta = 2\alpha^{array}$. Previously, the value of α^{array} was uniform across the 6R8R assembly, fixing the turning angle for a given assembly. However, the Arc Miura assembly is capable

of locally changing α^{array} to a range of values, allowing the geometry of the 6R linkage to be chosen more freely and thereby changing the folded state, as shown in Figure 24.

The combined assembly must have identical geometries at any overlapped region, and as such will locally follow the same mobility paths as described in Sections 3.1.1 and 3.2.1. The inserted 6R8R assembly can now be assigned a range of turning angles, limited only by the collision of panels. Figure 24 shows the new limits of the Arc Miura - 6R8R combination. The 8R arrays at each end of the assemblies are identical and have zero turning angle, but the Arc Miura linkages on either side of the central 6R linkages change the characteristic angle from with α^{array} to α^{6R}. α^{6R} can range between $\frac{\pi}{4} \leq \alpha^{6R} < \alpha^{array}$ and, through the relation $\delta = 2(2\alpha^{6R} - \alpha^{array})$, turning angles of $\pi - 2\alpha^{array} \leq \delta \leq 2\alpha^{array}$ are achieved.

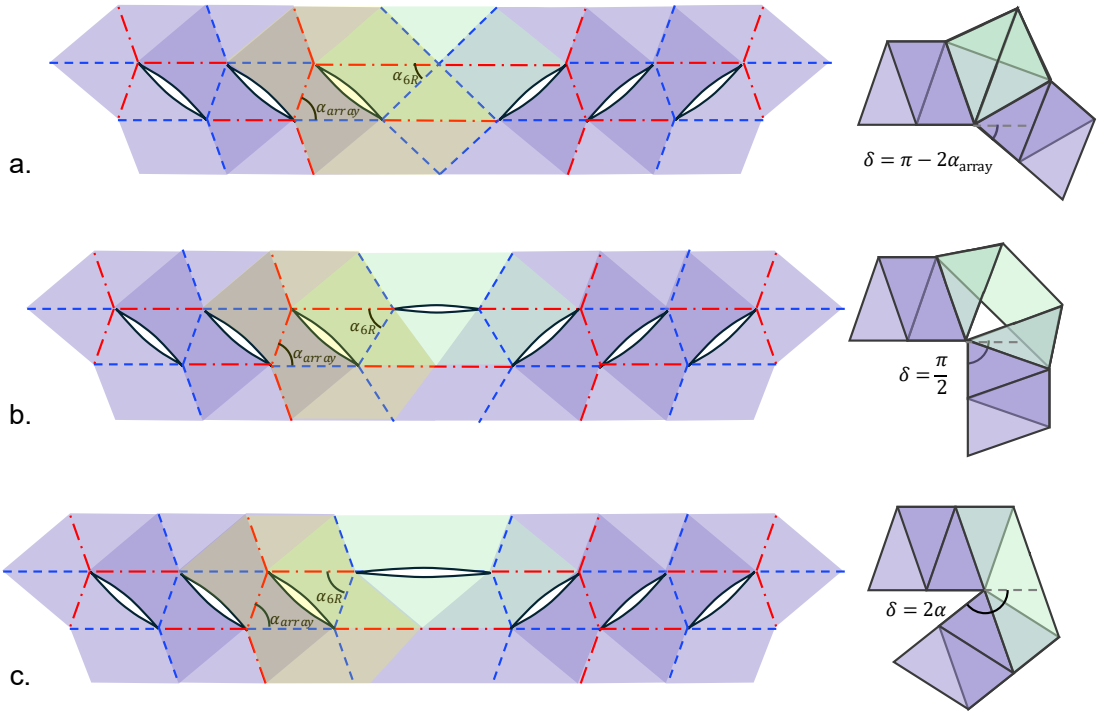

Figure 24a. An Arc 6R8R assembly with $\alpha^{array} = \frac{7\pi}{18}$, $\alpha^{6R} = \frac{\pi}{4}$, $\delta = \frac{2\pi}{9}$. b. An Arc 6R8R assembly with $\alpha^{array} = \frac{7\pi}{18}$, $\alpha^{6R} = \frac{23\pi}{72}$, $\delta = \frac{\pi}{2}$. c. An Arc 6R8R assembly with $\alpha^{array} = \frac{7\pi}{18}$, α^{6R} $\frac{7\pi}{18}$, $\delta = \frac{7\pi}{9}$.

4. Conclusion

Two new mechanisms have been demonstrated in this work, both with a level of customisability in their folded state. When used tandem, they can be used to produce mechanisms that conform to any continuous 2D function in their folded state and which deploy to a voidless flat surface, with a single degree of freedom. This result broadens the design toolbox for thick-panel deployable structures and allows truly custom folded form for given use cases.

References

[1] T. Chen, O. Bilal, R. Lang, C. Daraio and K. Shea, *Autonomous Deployment of a Solar Panel Using an Elastic Origami and Distributed Shape Memory Polymer Actuators,* 2018.

[2] M. Johnson, Y. Chen, S. Hovet, S. Xu, B. Wood, H. Ren, J. Tokuda and Z. T. H. Tse, "Fabricating biomedical origami: a state-of-the-art review," *International Journal of Computer Assisted Radiology and Surgery,* vol. 12, no. 11, pp. 2023-2032, November 2017.

[3] S. A. Zirbel, R. J. Lang, M. W. Thomson, D. A. Sigel, P. E. Walkemeyer, B. P. Trease, S. P. Magleby and L. L. Howell, "Accommodating thickness in origami-based deployable arrays1," *Journal of Mechanical Design,* vol. 135, no. 11, 2013.

[4] J. S. Ku and E. D. Demaine, "Folding flat crease patterns with thick materials," *Journal of Mechanisms and Robotics,* vol. 8, no. 3, June 2016.

[5] T. Tachi, "Rigid-Foldable Thick Origami," *Origami 5: Fifth International Meeting of Origami Science, Mathematics, and Education.,* 2011.

[6] Y. Chen, R. Peng and Z. You, "Origami of thick panels," *Science,* vol. 349, no. 6246, pp. 396-400, July 2015.

[7] C. Wang, J. Li, C. Wang, J. L. Li and Z. You, *A Kirigami-inspired Foldable Model for Thick Panels,* 2018.

[8] J. Yang, X. Zhang, Y. Chen and Z. You, "Folding arrays of uniform-thickness panels to compact bundles with a single degree of freedom," *Proceedings of the Royal Society A: Mathematical, Physical and Engineering Sciences,* vol. 478, no. 2261, 2022.

[9] J. Denavit and R. S. Hartenberg, "A Kinematic Notation for Lower-Pair Mechanisms Based of Matrices," *Applied Mechanics,* 1955.

[10] C. Liu, Z. You and P. Maiolino, *KINEMATICS OF AN ORIGAMI INSPIRED MILLIPEDE ROBOT,* 2022.

[11] D. Xing and Z. You, "Kinematic behaviour of origami combining two four-crease vertices," *Mechanics Research Communications,* vol. 134, 2023.

[12] C. Hoberman, "Folding structures made of thick hinged sheets". 14 September 2010.

[13] B. J. Edmondson, R. J. Lang, S. P. Magleby and L. L. Howell, "An Offset Panel Technique for Thick Rigidily Foldable Origami," 2014.

5. Appendix

A 4R linkage assembly was designed in this work, however it does not have much relevance to the other linkages, so is presented in this appendix for the reader's interest. The assembly is a single DOF, monohedral, plane tiling mechanism that has a folded and unfolded state without holes. This assembly is based on a simple planar 4 bar linkage, linking 4 panels together, shown in Figure 25. Each panel is the union of two squares, offset by half a side length. Since all the Z^{4R} axes are parallel, kinematics of this linkage are trivial, with the loop closure equation being: $\varphi_1^{4R} = \varphi_2^{4R} = \varphi_3^{4R} = \varphi_4^{4R}$.

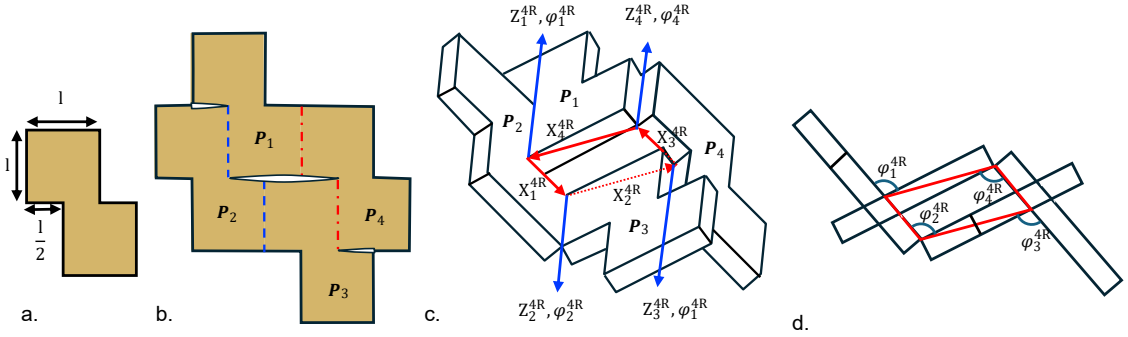

Figure 25a. 4R panel geometry. b. 4R linkage arrangement. c. 3D view of 4R linkage with DH axes shown. d. Plan view of the 4R linkage.

The assembly can be tiled to cover a large area, as demonstrated in Figure 26a, which folds up with a single degree of freedom and can also tesselate with similar assemblies in their compact state.

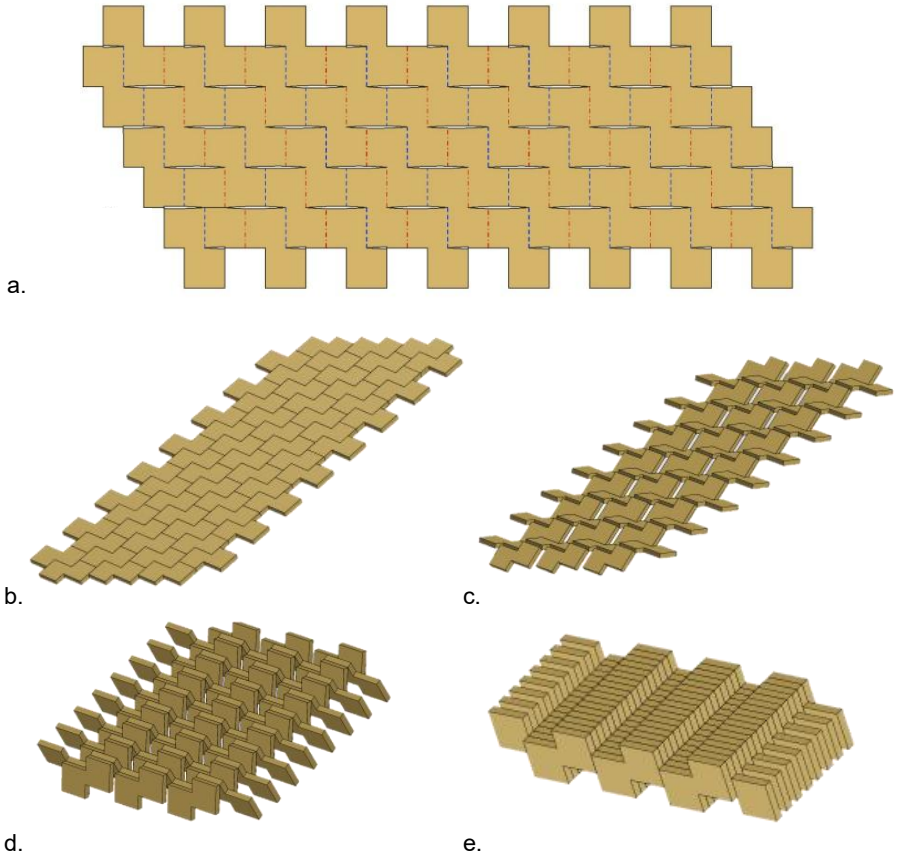

Figure 26a. Layout of a large 4R linkage assembly. b-e. The assembly folding up to its compact state.